Numerical investigation of tunnelling effects on existing piles in structured clay

Jun-Xiu Liu, Jie Yang, Ying-Jing Liu, Shu Zhu, Farid Laouafa

Numerical investigation of tunnelling effects on existing piles in structured clay

Jun-Xiu LIU[1,2], Jie YANG[3,4,*], Ying-Jing LIU[5], Shu ZHU[6], Farid LAOUAFA[7]

- Jun-Xiu LIU, Ph.D., Associate professor

[1] Anhui Province Key Laboratory of Building Structure and Underground Engineering, Anhui Jianzhu University, Hefei, Anhui 230601, China

[2] College of Civil Engineering, Anhui Jianzhu University, Hefei, Anhui 230601, China

Email: tju_liu@hotmail.com

- Jie YANG, Ph.D.

[3] Department of Civil and Environmental Engineering, The Hong Kong Polytechnic University, Hung Hom, Kowloon, Hong Kong, China

[4] Laboratory of Geomaterials and Modelling in Geotechnics, Department GERS, University Gustave Eiffel, Bouguenais, France

Corresponding author, Email: doc.jie.yang@gmail.com

- Ying-Jing LIU, Ph.D.

[5] Zhongtian Construction Group Co. Ltd., Hangzhou, China

Email: 386005244@qq.com

- Shu ZHU, Ph.D.

[6] College of Civil Engineering, Hunan University, Changsha, Hunan 410082, China

Email: zhushu@hnu.edu.cn

- Farid LAOUAFA, Ph.D., Director of research

[7] National Institute for Industrial Environment and Risks (INERIS), Verneuil-en-Halatte, France

Email: farid.laouafa@ineris.fr

Numerical investigation of tunnelling effects on existing piles in structured clay

Jun-Xiu LIU[1,2], Jie YANG[3,4,*], Ying-Jing LIU[5], Shu ZHU[6], Farid LAOUAFA[7]

Affiliations:

[1] Anhui Province Key Laboratory of Building Structure and Underground Engineering, Anhui Jianzhu University, Hefei, Anhui 230601, China

[2] College of Civil Engineering, Anhui Jianzhu University, Hefei, Anhui 230601, China

[3] Department of Civil and Environmental Engineering, The Hong Kong Polytechnic University, Hung Hom, Kowloon, Hong Kong, China

[4] Laboratory of Geomaterials and Modelling in Geotechnics, Department GERS, University Gustave Eiffel, Bouguenais, France

[5] Zhongtian Construction Group Co. Ltd., Hangzhou, China

[6] College of Civil Engineering, Hunan University, Changsha, Hunan 410082, China

[7] National Institute for Industrial Environment and Risks (INERIS), Verneuil-en-Halatte, France

*Corresponding author: Dr. Jie YANG, Department of Civil and Environmental Engineering, The Hong Kong Polytechnic University, Hung Hom, Kowloon, Hong Kong, China; Laboratory of Geomaterials and Modelling in Geotechnics, Department GERS, University Gustave Eiffel, Bouguenais, France ; Email: doc.jie.yang@gmail.com

Abstract: Tunnel construction may induce ground deformations and affect the adjacent pile foundations. Up to now, few studies have investigated the soil-tunnel-pile interaction in structured clay. In this study, an anisotropic structured clay model is implemented in the finite-difference code FLAC^{3D} to investigate the effects of tunnelling on existing piles in structured clay. The model is first calibrated based on the oedometer and undrained triaxial test results for Shanghai structured clay. Then the finite difference model and the modelling procedure are introduced and validated by simulating the centrifuge model tests of tunnelling adjacent to piles in remoulded kaolin clay. Thereafter, influences of clay anisotropy and structure on the existing

piles due to tunnelling are investigated using the calibrated parameters for Shanghai structured clay. It is observed that the influence of clay structure on the shape of the deflection and bending moment of the pile is not significant. However, the introduction of the anisotropy and the adhesive mean stress may reduce the ground settlement while increasing the lateral soil movement at the tunnel axis depth, whereas the introduction of the bonding ratio may have the opposite effect. Moreover, introducing both the anisotropy and the soil structure will lead to the increase of pile moment.

Keywords: tunnelling; pile; clay; soil structure; finite difference method; bounding surface model

1. Introduction

Tunnels are considered to be one of the most widely used underground structures. The construction, maintenance and the induced influences on the surrounding soils and structures have been widely studied experimentally and numerically(Jiang & Yin, 2012, 2014; Li, Du, Ma, Yin, & Shen, 2014; Shen, Wu, Cui, & Yin, 2014; Wongsaroj, Soga, & Mair, 2013; Wu, Shen, Chai, Zhang, & Xu, 2014; J. Yang, Z.-Y. Yin, F. Laouafa, & P.-Y. Hicher, 2019a, 2019b, 2019c; J. Yang, Z. Y. Yin, F. Laouafa, & P. Y. Hicher, 2019; Zhang, Huang, Yin, Ran, & Huang, 2017). In densely built cities, tunnel construction will inevitably cause soil deformation and stress relief, which may induce adverse effects on nearby existing piles. To accurately predict the effects of tunnelling on existing piles, a series of studies have been carried out to investigate the soil-tunnel-pile interaction mechanism in dry sand (Hong, Soomro, & Ng, 2015; Lu, Shi, Ng, & Lv, 2020; Marshall & Mair, 2011; Ng, Hong, & Soomro, 2015; Ng & Lu, 2014; Ng, Soomro, & Hong, 2014; Soomro, Mangi, Xiong, Kumar, & Mangnejo, 2020; Z.-Y. Yin, Xu, & Hicher, 2013). Moreover, centrifuge model tests and numerical simulations have been performed to study the effects of tunnelling on adjacent piles in remoulded kaolin clay or stiff clay (N. Loganathan, Poulos, & Stewart, 2000; Soomro, Hong, Ng, Lu, & Peng, 2015; Soomro, Kumar, Xiong, Mangnejo, & Mangi, 2020; Soomro, Ng, Liu, & Memon, 2017; Williamson, Elshafie, Mair, & Devriendt, 2017; Williamson, Mair, Devriendt, & Elshafie, 2017).

However, it is well recognised that the properties of naturally deposited clays are significantly different from the remoulded clay because of the progressive destructuring of natural clay during plastic straining (Clayton, Hight, & Hopper, 1992; Leroueil & Vaughan, 1990). Previous studies on soil-tunnel-pile interaction were mostly focused on the soil-tunnel-pile interaction mechanism in sand or remoulded clay. The experimental studies on the effects of

tunnelling on existing piles in structured clay have been rarely reported, which may be due to the difficulties in the preparation of structured clay samples in the model tests. Meanwhile, in terms of numerical studies, the commonly used numerical analysis programmes for geotechnical engineering (such as FLAC, PLAXIS, ZSOIL, etc.) do not contain any built-in structured clay constitutive models, the effects of tunnelling on existing piles in structured clay are therefore not well understood.

Recently, some constitutive models that can capture the features of the structured soil have been proposed (Huang, Liu, & Sheng, 2011; Liu & Carter, 2002; Wheeler, Näätänen, Karstunen, & Lojander, 2003; Yang, Yin, Liu, & Gao, 2020; Z.-Y. Yin, Chang, Karstunen, & Hicher, 2010; Z.-Y. Yin, Karstunen, Chang, Koskinen, & Lojander, 2011), which made it possible to numerically investigate the effects of tunnelling on existing piles. In this study, an anisotropic structured clay model (ASCM) is briefly presented and improved by introducing three degrees of disturbance for clay anisotropy and structure. It is implemented into the finite difference programme FLAC^{3D} through a user-defined constitutive model platform using the coding language of C++. Then, a series of undrained triaxial tests and an oedometer test on Shanghai structured clay are simulated to calibrate the ASCM model parameters. Thereafter, by using the user-defined ASCM model in FLAC^{3D}, the finite difference model and the modelling procedure for simulating tunnelling effects on existing piles are introduced and validated by modelling the centrifuge model tests of tunnelling adjacent to piles in remoulded kaolin clay performed by N. Loganathan, Poulos, and Stewart (2000). On this basis, the influences of soil anisotropy and structure on soil-tunnel-pile interaction are further investigated using the validated 3D finite difference model.

2. Implementation of ASCM into FLAC^{3D}

2.1. Introduction of Anisotropic Structured Clay Model – ASCM

In this study, the Anisotropic Structured Clay Model (ASCM) proposed by Yang, Yin, Liu, and Gao (2020) has been adopted and improved by introducing three degrees of disturbance of clay anisotropy and structure. The model was developed under the framework of critical state concept and bounding surface plasticity.

The main constitutive equations can be found in the Appendix. The parameters of the ASCM model can be calibrated from triaxial and oedometer tests, and are mainly divided into three groups:

(1) The Modified Cam-Clay (MCC) analogous parameters (λ, κ, M_c, υ) and the initial state parameters (p_{c0}, e_0) can be determined from conventional triaxial and oedometer tests. p_{c0} can be replaced by the pre- overburden pressure (*POP*).

(2) The structured parameters (ξ, ξ_d, ξ_b) and initial state parameters (χ_0, p_{b0}) can be determined by comparing triaxial compression and one-dimensional compression tests.

(3) The parameters for plastic modulus (k_p) can be obtained by best fitting the experimental results of triaxial compression tests on over-consolidated clay.

If $\chi_0 = p_{b0} = 0$, the ASCM model degenerates to the S-Clay1 model (Wheeler, Näätänen, Karstunen, & Lojander, 2003). If $\chi_0 = p_{b0} = \alpha_{K_0} = 0$, the ASCM model degenerates to the MCC model.

It should be noted that, due to the measurement error and the discrepancies of experimental results, the parameters are not easy to be quantified accurately by the standard way. Another efficient procedure for parameter identification is to apply the recently developed optimisation methods (Y.-F. Jin, Yin, Zhou, & Huang, 2019; Y. F. Jin, Yin, Shen, & Hicher, 2016; Z.-Y. Yin, Jin, Shen, & Huang, 2017; Z. Y. Yin, Jin, Shen, & Hicher, 2018) or Bayesian-based methods (Y.-F. Jin, Yin, Zhou, & Horpibulsuk, 2019; Y. F. Jin, Yin, Zhou, & Shao, 2019).

2.2. Model implementation in FLAC^{3D}

The ASCM model has been implemented in the finite difference code FLAC^{3D} (Itasca Consulting Group Inc., 2018), through a compiled DLL file. The general calculation cycle with a user-defined constitutive model in FLAC^{3D} is shown in Figure 1. This procedure first invokes the equations of motion to derive new velocities and displacements from stresses and forces. Then, strain rates are derived from velocities. Thereafter, it is the role of the compiled DLL file to update the effective stress, the state variables and the hardening parameters, given their old set of values and the applied strain rates.

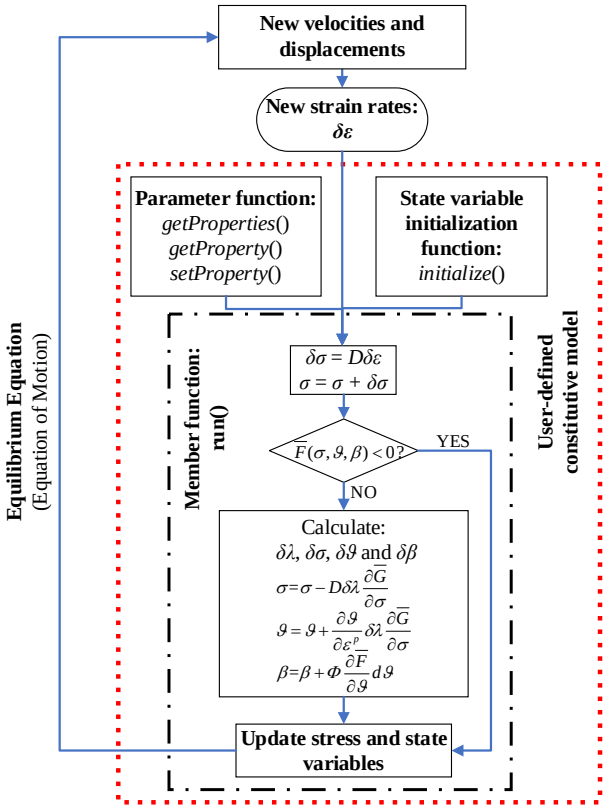

Figure 1 General calculation cycle with a user-defined constitutive model in FLAC^{3D}

The foregoing procedure is code-related and will not be elaborated further. What is not code-related is the stress integration scheme employed ASCM model. Figure 1 also shows the detailed user development process of the ASCM model. Material parameter assignment and reading is achieved through three member functions: *getProperties*(), *getProperty*() and *setProperty*(). The member function *getProperties*() returns a string containing the names of model properties. The *getProperty*() returns a value for the model property of sequence number *n* previously defined by a *getProperties*() call, with *n*=1 denoting the first property. The *setProperty*() is used to set the value of dVal supplied by the call comes from a FLAC^{3D} command of the form PROP name=dVal. The member function of *initialize*() is used to perform the initialization of constitutive model property or state variables. The *initialize*() function is called once for each full zone when the FLAC^{3D} CYCLE command is given. The member function *run*() is to compute new stresses from strain increments with updating state variables. Within each calculation cycle or step, the *run*() function is called by FLAC^{3D} ten times (once for each subzone) for each hexahedral zone, which is internally discretized into 2 overlays.

In this study, the explicit algorithm has been adopted for plastic correction. The detailed stress integration scheme and main steps of member function *run*() are as follows:

(1) trial calculation:

$$\sigma_{i+1} = \sigma_i + \delta\sigma^e = \sigma_i + D\delta\varepsilon \quad \text{..... (1)}$$

(2) If $\overline{F}\left(\sigma_{i+1}, \vartheta, \beta\right) \le 0$, the trial result can be directly assigned to the subzone. If $\overline{F}\left(\sigma_{i+1}, \vartheta, \beta\right) > 0$, the updated stress point is outside the yield surface, stress correction should be performed as follows:

① The consistency principle of the elastoplastic theory was adopted to calculate the plastic multiplier ($\delta\lambda$):

$$\delta\lambda = \frac{-\frac{\partial\overline{F}}{\partial\sigma} D\delta\varepsilon}{-\frac{\partial\overline{F}}{\partial\sigma} D \frac{\partial\overline{G}}{\partial\sigma} + \left(1 + \frac{\partial\overline{F}}{\partial\beta}\Phi\right)\frac{\partial\overline{F}}{\partial\vartheta}\frac{\partial\vartheta}{\partial\varepsilon^p}\frac{\partial\overline{G}}{\partial\sigma}} \quad \text{..... (2)}$$

② Calculate plastic strain increments ($\delta\varepsilon_{ij}^{\mathrm{p}}$) according to Equation (A16);

③ Update stress by:

$$\sigma_{i+1} = \sigma_i + D(\delta\varepsilon - \delta\varepsilon^{\mathrm{p}}) \quad \text{..... (3)}$$

④ Update hardening parameters by:

$$\vartheta_{i+1} = \vartheta_i + \frac{\partial\vartheta}{\partial\varepsilon^{\mathrm{p}}}\delta\lambda\frac{\partial\overline{G}}{\partial\sigma} \quad \text{..... (4)}$$

⑤ Update mapping coefficient by:

$$\beta_{i+1} = \beta_i + \Phi\frac{\partial\overline{F}}{\partial\vartheta}d\vartheta \quad \text{..... (5)}$$

3. Model calibration for Shanghai structured clay

The model parameters for Shanghai structured clay are calibrated based on the oedometer test and the undrained triaxial test results carried out by Huang, Liu, and Sheng (2011) on Shanghai structured clay. A numerical model of one zone cube with 1.0 m in dimension was established by FLAC^{3D} for model calibration for Shanghai structured clay. By applying optimization-based methods (Z.-Y. Yin, Jin, Shen, & Huang, 2017), the material parameters for Shanghai clay are

calibrated from the oedometer test and isotropically consolidated undrained triaxial tests (shown in Table 1) and used to predict the behaviours of anisotropically consolidated specimens (K_0 = 0.6) under triaxial loadings. The numerical results obtained by using the ASCM model are compared with those of the MCC model.

Table 1 Model parameters for Shanghai clay

λ	κ	M_c	p_{c0} / kPa	e_0	υ	χ_0	ξ	ξ_d	p_{b0} / kPa	ξ_b	POP / kPa
0.17	0.036	1.04	69.0	1.37	0.25	4.8	11.0	0.32	18.5	2.0	24.6

Figure 2 to Figure 4 present the comparison between the results of the ASCM model, MCC model and the experimental data for the oedometer test and undrained triaxial tests on Shanghai structured clay. It can be seen that the implemented ASCM model can well reproduce the difference in compression characteristics before and after the damage of soil structure. The predicted effective stress paths converge towards the critical state line, and the characters of high stiffness and strain softening for structured clay are also well reflected by the implemented ASCM model, whereas the prediction of the MCC model for structured clay was less satisfactory.

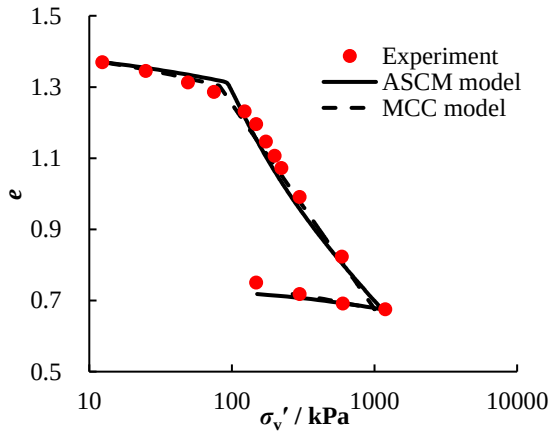

Figure 2 Simulation of oedometer test on Shanghai clay

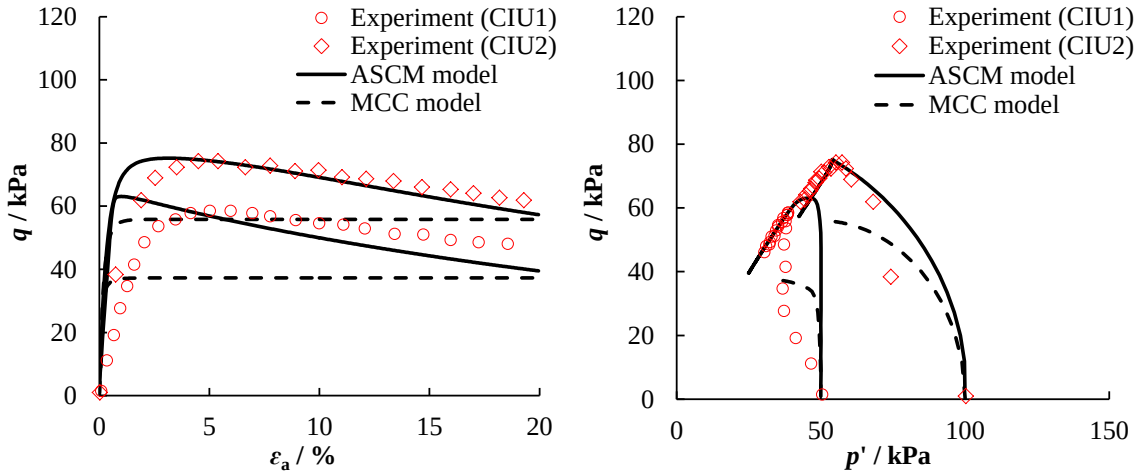

(a) deviatoric stress versus axial strain (b) deviatoric stress versus mean effective stress

Figure 3 Simulation of undrained triaxial tests on isotropically consolidated Shanghai structured clay

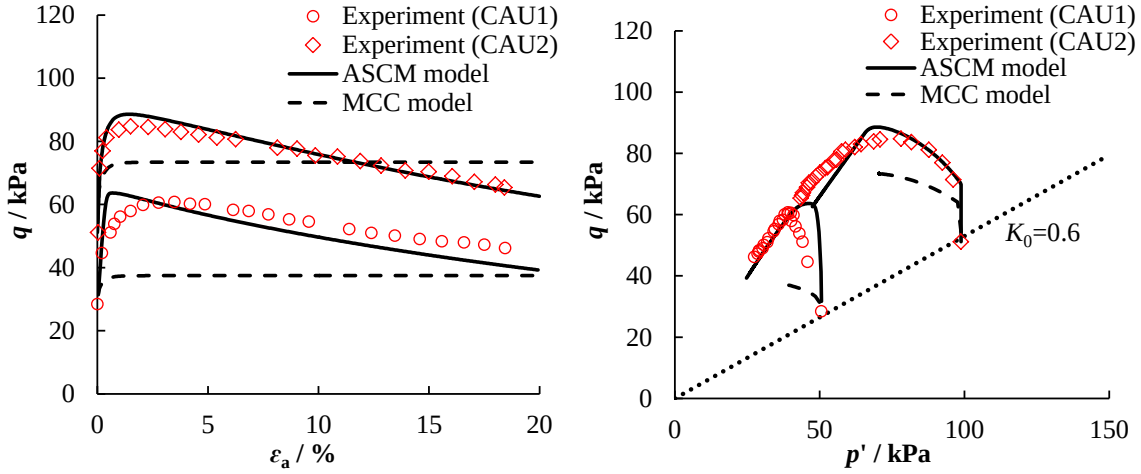

(a) deviatoric stress versus axial strain (b) deviatoric stress versus mean effective stress

Figure 4 Simulation of undrained triaxial tests on K_0 consolidated Shanghai structured clay

4. Simulation of centrifuge tests of tunnelling in remoulded kaolin clay

4.1. Description of the tests

N. Loganathan, Poulos, and Stewart (2000) performed three centrifuge model tests with different tunnel buried depths to investigate the effects of tunnelling on adjacent piles in remoulded kaolin clay. The tests were carried out at a centrifuge acceleration of 100g. The layout and dimensions of the centrifuge model are shown in Figure 5.

In the centrifuge model test, the clay sample had a plan dimension of 650 mm × 200 mm and a depth of 300mm. The tunnel model consisted of an inner core made of an aluminium tube and an outer rubber membrane wrapping around the core. The annulus between the inner core and the membrane was filled with silicon oil. The outer diameter of the tunnel is 60 mm. Depth

to the tunnel centre-line was varied (H = 15, 18 and 21 m represent the distance from the ground surface to the tunnel axis). A single pile and a 2 × 2 pile group were installed respectively on either side of the tunnel. The model pile group had a centre-to-centre spacing of 25 mm. The distance from the axis of the model tunnel to the single pile and the front pile in the group was 55 mm. The model piles were made of brass tubes to simulate 0.8 m diameter circular concrete piles. The outer diameter and internal diameter of the model piles were 8 mm and 7.24 mm, respectively. The length of the model piles was 180 mm.

The kaolin clay was mixed with slurry under vacuum conditions and then consolidated under constant vertical effective stress (600 kPa) at 1g condition. The tunnel excavation was modelled by extracting a controlled amount of silicone oil in-flight to achieve the specified equivalent ground loss value (1.0%). The ground surface settlements, the subsurface movements, and the pile lateral deflections were measured during the centrifuge flight.

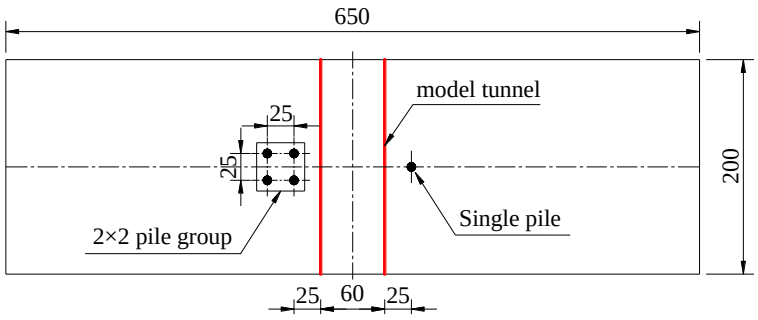

(a) Plan view (dimensions in mm)

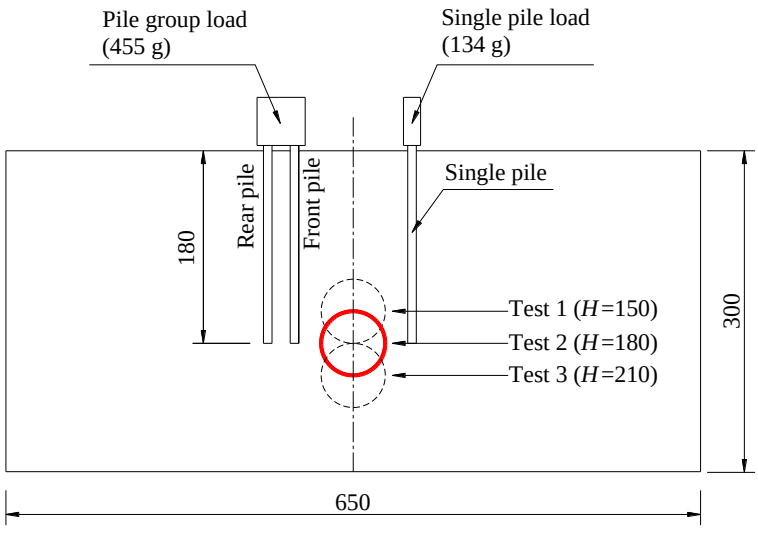

(b) Elevation view (dimensions in mm)

Figure 5 Detail and geometry of the centrifuge model (N. Loganathan, Poulos, & Stewart, 2000)

4.2. Numerical model

Figure 6 shows an isometric view of the numerical model (for the case of H = 18 m) in FLAC^{3D} in accordance with the prototype model. The pile group load (zone A) and single pile load (zone B) were modelled by hexahedral brick elements with 4.5 m × 4.5 m × 4.5 m and 1.6 m × 1.6 m × 5.0 m in dimensions, respectively. According to the law of similarity, the mass of zone A and zone B in the numerical model was set to 4.55×10^5 kg and 1.34×10^5 kg, equivalent to a deadweight of 4.55 MN and 1.34 MN applied to the top of the 2 × 2 pile group and the single pile. The boundary conditions were taken as rollers on the vertical boundary surfaces of the model and as fully fixed at the base of the model. The groundwater level was supposed to be located at the ground surface.

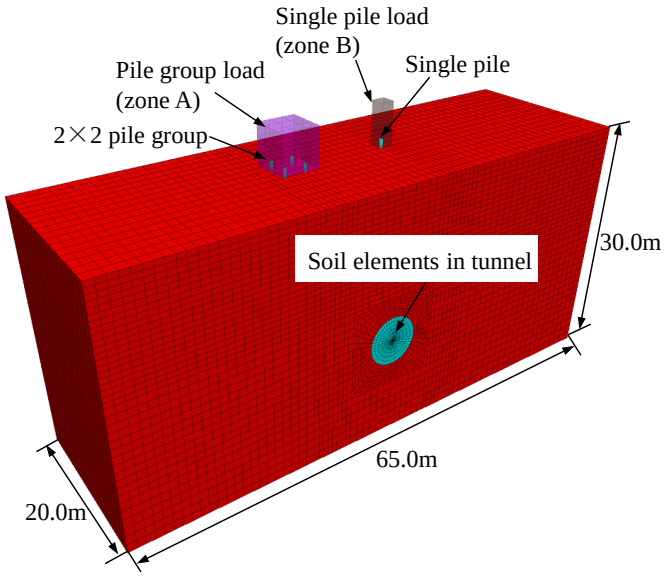

(a) Finite difference mesh

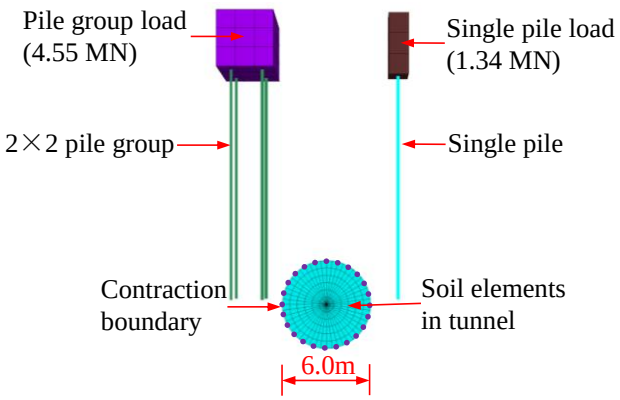

(b) Tunnel and piles

Figure 6 Numerical model of the tunnel and piles (for the case of test 2, H = 18 m)

4.3. Model parameters

The kaolin clay was modelled by the implemented ASCM model with parameters summarized in Table 2. The parameters for clay are adopted from Divall (2013) except for the pre-overburden pressure (*POP*), which is deduced based on the undrained shear strength of the tested kaolin clay.

Figure 7 shows the undrained shear strength measured by the vane shear tests immediately after the three centrifuge model tests and that computed by undrained triaxial tests simulation by FLAC^{3D} with parameters in Table 2. In the undrained triaxial tests simulation, the initial stress corresponds to the initial stress state at different depths of the clay foundation with the pre-overburden pressure (*POP*) equal to 600 kPa. However, it was found that the computed undrained shear strength with *POP* equal to 600 kPa was significantly greater than the shear strength measured in the centrifuge model test. According to N. Loganathan, Poulos, and Stewart (2000), the discrepancy was due to the disturbances of clay during the model set-up, including the swelling of the clay, cylindrical cavity excavation of the model tunnel, the pile installation, etc. Besides, the kaolin soil experienced a complex stress path, including the consolidation under constant pressure (600 kPa) at 1g condition and then the consolidation under self-weight at 100g centrifuge acceleration. By carrying out a back analysis, it was found that the computed undrained shear strength could match well with the measurements when *POP* was set to 300 kPa.

Table 2 Material properties of the foundation

Description	Parameter
Saturated unit weight (kN·m^{-3}): γ_{sat}	17.5
Intrinsic compression index (of remoulded soil): λ	0.18
Intrinsic swelling index (of remoulded soil): κ	0.035
Slope of the critical state line in the p′-q plane: M_c	0.89
Initial void ratio: e_0	1.27
Poisson's ratio: υ	0.25
Plastic modulus-related parameter in the bounding surface: k_p	500
Initial bonding ratio: χ_0	0
Degradation rate of the bonding ratio related to the plastic volumetric strain: ξ	0
Degradation rate of the bonding ratio related to the plastic deviatoric strain: ξ_d	0

Initial inter-particle bonding : p_{b0}	0
Degradation rate of the inter-particle bonding: ξ_b	0
Pre-overburden pressure (kPa): POP	300

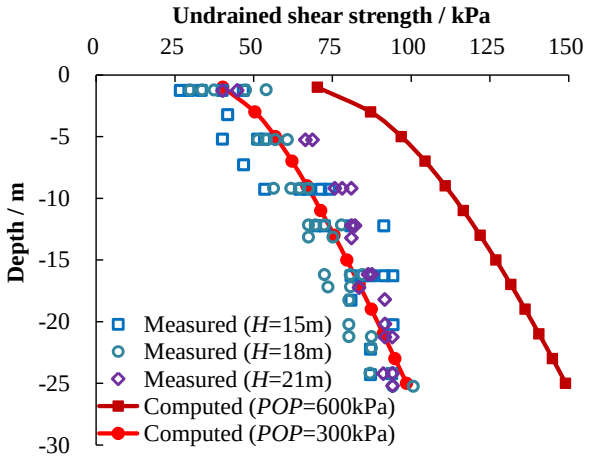

Figure 7 Measured and computed undrained shear strength profiles of the clay

Accordingly, the initial size of the yield surface p_{c0} and the intrinsic yield surface p_{ci0} of naturally deposited clays varies with depth and can be determined by Equation (A13) and (A14).

The structural pile element inherent in FLAC^{3D} was used to simulate the piles, which were modelled as elastic material with Young's modulus of 30 GPa and Poisson's ratio of 0.25. The diameter of the circular concrete piles is 0.8 m. The brick elements for pile loads (zone A and zone B) that played the role of pile cap were assumed to be linear elastic with Young's modulus of 70 GPa and Poisson's ratio of 0.2. All piles were assumed to be rigidly connected to zone A or zone B.

The interaction between piles and soil was defined by the normal and shear coupling springs, which is cohesive and frictional in nature. According to (N. Loganathan, Poulos, and Xu (2001)), the pile-soil interface has a friction of φ_i = 0, and cohesive strength of c_i = 75 kPa. Therefore, the friction angle of the coupling spring is 0, and the normal and shear coupling spring cohesion per unit length is 188.4 kN/m. The coupling spring stiffness can be set to ten times the equivalent stiffness of the stiffest neighbouring zone (Itasca Consulting Group Inc., 2018). Therefore, the normal and shear coupling spring stiffness per unit length of the pile can be calculated by using Equation (6):

$$k_n = k_s = 10 \times \max\left[\frac{K + \frac{4}{3}G}{\Delta z_{min}}\right] \cdot d \quad \text{..... (6)}$$

where k_n and k_s are the normal and shear coupling spring stiffness per unit length, respectively; K and G are the bulk modulus and shear modulus of the kaolin clay in this study; $\Delta z_{min} = 0.625$ m is the smallest dimension of an adjoining zone in the normal direction; $d = 2.512$ m is the perimeter of the pile. The 'max[ ]' notation indicates the maximum value overall zones adjacent to the pile. Therefore, $k_n = k_s = 493$ MPa were obtained and used in this study.

4.4. Modelling procedure

The numerical simulation procedures were the same as the centrifuge tests: (1) Define the material properties of the numerical model; (2) Initiate the boundary and initial stress conditions, and the initial equilibrium state; (3) Activate the piles and the pile loads on top of the piles, and calculate to the equilibrium state; (4) Simulate tunnel excavation by deactivating the elements in the tunnel and stepping the solution of non-uniform boundary contraction.

Figure 8 shows the non-uniform boundary contraction (Lee, Rowe, & Lo, 1992) due to ground loss during tunnelling. The maximum inward displacement of the excavated surface (δ_{max}) appears at the tunnel crown, and zero displacement occurs at the invert. The non-uniform inward displacement can be calculated as:

$$\delta = \sqrt{R^2 - 2R \cdot \Delta \cdot \cos(\theta + \pi/2) + \Delta^2} - R_0 \quad \text{..... (7)}$$

where R_0 is the radius of the converged surface, R is the radius of excavated surface, θ is the angle of the polar coordinate system with the origin located at the centre of excavation; Δ is the distance between excavation centre and convergence centre. Table 3 summarizes the parameters of the non-uniform boundary contraction for simulating the 1.0% equivalent ground loss. The application of the non-uniform inward displacement was achieved by a function written in FISH language embedded in FLAC^{3D}.

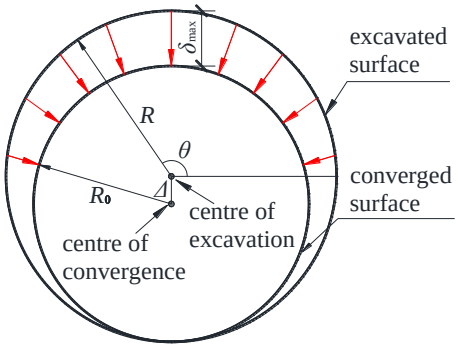

Figure 8 Non-uniform boundary contraction model

Table 3 Parameters of the non-uniform boundary contraction model

R / m	R_0 / m	δ_{max} / m	Δ / m
3.0	2.9850	0.030	0.0150

4.5. Numerical results

In this section, the ground and pile deformations measured from the centrifuge tests are compared and discussed with the numerical simulation results in terms of prototype units.

Figure 9 shows the measured and computed ground surface settlement induced by tunnelling. It can be seen that the ground surface deforms like a "V". The maximum settlement is located at the vertical axis of the tunnel and decreases slightly with the increase of the tunnel buried depth. For the cases of H = 18 m and 21 m, the computed profiles of ground surface settlement using the ASCM model agree reasonably well with the measurements. In the case of H = 15 m, the computed surface settlement at the tunnel centre-line is relatively smaller than the measurements. This is because the measured results for planned 1.0% ground loss for the case of H = 15 m were obtained by linear interpolation of other ground loss results, due to the leakage of silicone oil from the model tunnel during the consolidation spin, which caused the initial diameter of the model tunnel to be reduced (N. Loganathan, Poulos, & Stewart, 2000).

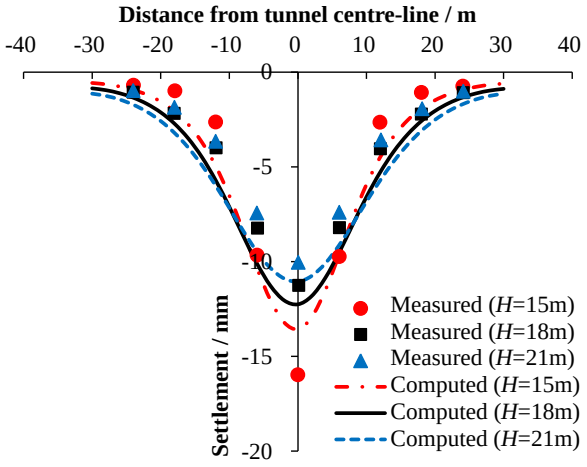

Figure 9 Measured and computed ground surface settlement induced by tunnelling for different tunnel buried depths

Figure 10 shows the measured and computed subsurface settlement along the tunnel axis in the vertical direction. It is observed that the shape of the subsurface settlement can be well captured by numerical modelling. The maximum subsurface settlement appears at the depth of the tunnel crown, equal to the maximum displacement of the non-uniform boundary contraction of the excavated surface. The ground subsurface settlement decreases when approaching the ground surface.

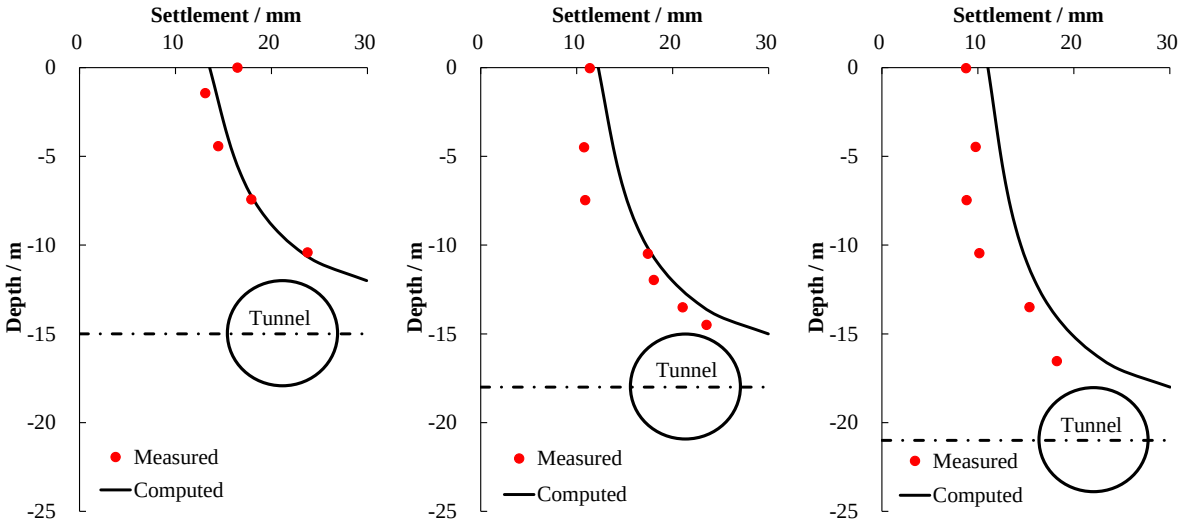

(a) H=15 m (b) H=18 m (c) H=21 m

Figure 10 Measured and computed subsurface settlement of the ground induced by tunnelling

Figure 11 compares the measured and computed lateral soil movements at a horizontal distance of 5.5 m from the tunnel axis. Positive lateral movements indicate that the soil deforms towards the tunnel. It can be seen that the computed shape agrees reasonably well with the measurements. The shape of the soil lateral movements is like an "S". However, the computed lateral soil movement is greater than the measurement for the case of H = 15 m, which is also caused by the interpolation of the measured results due to the leakage of silicone oil in the centrifuge test (N. Loganathan, Poulos, & Xu, 2001).

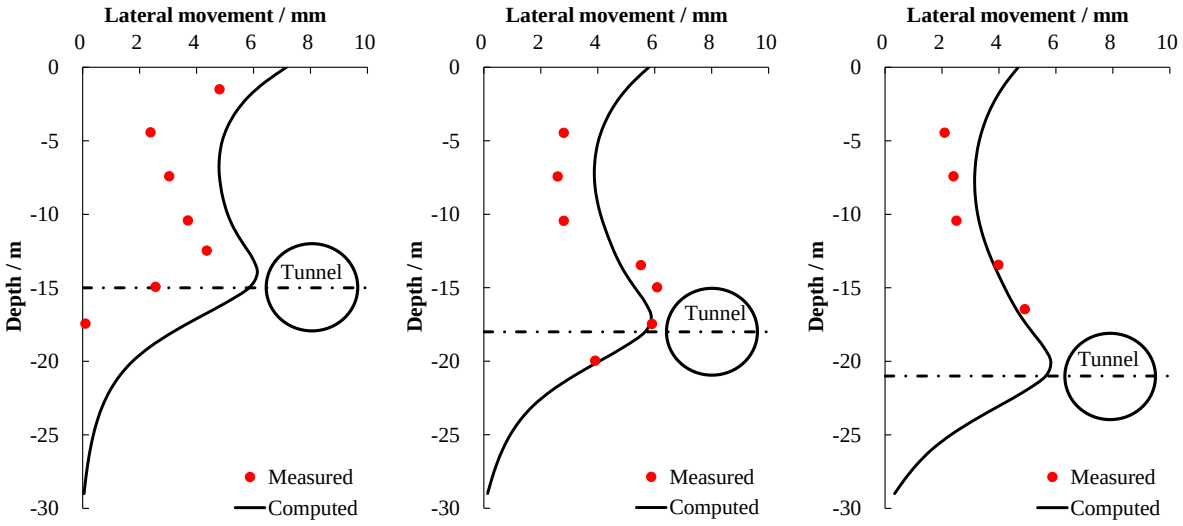

(a) H=15 m (b) H=18 m (c) H=21 m

Figure 11 Measured and computed lateral soil movements induced by tunnelling at different depths

Due to the lateral movements of the soil induced by tunnelling, piles embedded in the ground deformed laterally. Figure 12 shows the computed and measured lateral movements of the single pile, and the front and rear piles of the pile group for different tunnel depths. Positive lateral movements mean the pile deforms towards the tunnel. It is observed that for the cases of H = 18 m and 21 m, the computed pile deflection shapes and pile lateral movements match very well with the measured results. The maximum lateral movements of all the piles occur near the depth of the pile tips. As for the case of H = 15 m, the computed maximum lateral movements match with the measured results reasonably, however, discrepancies are observed in terms of the pile deflection shape between the measured and computed results. This is also due to the measured pile lateral movements for the case of H = 15 m were obtained by linear interpolation of other ground loss results (N. Loganathan, Poulos, & Stewart, 2000).

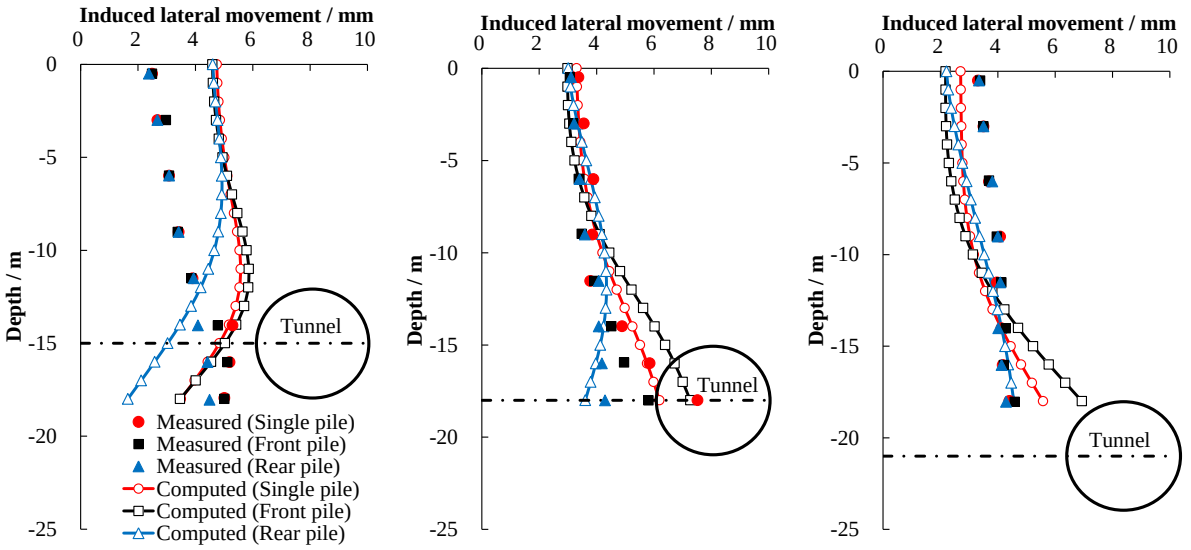

(a) H=15 m (b) H=18 m (c) H=21 m

Figure 12 Measured and computed plie lateral movements induced by tunnelling at different depths

Comparisons of the measured and computed results of the ground surface settlements, subsurface settlements, soil and pile lateral movements induced by tunnelling demonstrated that the established three-dimensional numerical models and the implemented ASCM model are reasonable in analyzing the influence of tunnel excavation on existing piles in clay. In the next section, the effects of tunnelling on existing piles in Shanghai structured clay will be further investigated. The influences of soil structure will be discussed.

5. Analysis of tunnelling in Shanghai structured clay

In this section, the influences of clay anisotropy and structure on the existing piles due to tunnelling are investigated using the calibrated parameters of Shanghai structured clay.

5.1. Numerical results

Figure 13 shows the bending moment profiles of the piles induced by tunnelling at different depths in Shanghai structured clay. Positive and negative bending moments denote the pile bends towards and away from the tunnel, respectively. As shown in Figure 13, the bending moment profiles of the single pile are similar to those of the front pile. For the rear pile which is relatively far away from the tunnel, the maximum bending moments are smaller than those of the single and front piles.

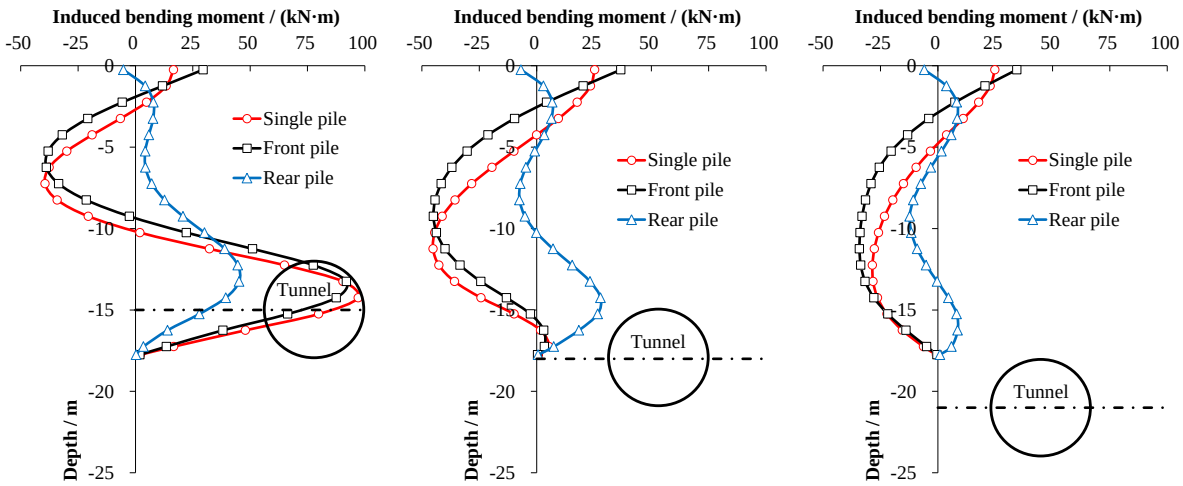

(a) H = 15 m (b) H = 18 m (c) H = 21 m

Figure 13 Bending moments of piles induced by tunnelling in Shanghai structured clay

Moreover, it is observed that when the depth of the tunnel axis is smaller than the pile length (i.e. the case of H = 15 m), the absolute maximum bending moment is positive and located at the depth of the tunnel. This is due to the tunnelling-induced stress-release at the tunnel depth. The maximum bending moments of the single pile and the front pile are around 100 kN·m, and the maximum bending moment of the rear pile is around 45 kN·m.

When the tunnel axis depth is equal to or greater than the pile length (i.e. the case of H = 18 m and 21 m), the single and front piles bends away from the tunnel, the absolute maximum bending moments are located in the mid-depth of the pile shaft as the pile tip move towards the tunnel. Compared to the case of H = 15 m, the maximum bending moments of the single and front piles for the case of H = 21 m are decreased by about 65% from around 100 kN·m to 35 kN·m.

Figure 14 shows the simulated plastic deviator strain contours induced by tunnelling at different depths in Shanghai structured clay. It can be seen that the distribution and magnitude of the plastic deviator strain for different tunnel buried depths are similar. The maximum plastic deviator strains corresponding to H = 15, 18 and 21 m are 1.45%, 1.28% and 1.21%, respectively. The maximum plastic deviator strain occurs at the shoulders on both sides of the tunnel crown and extends to the pile tips on both sides of the tunnel.

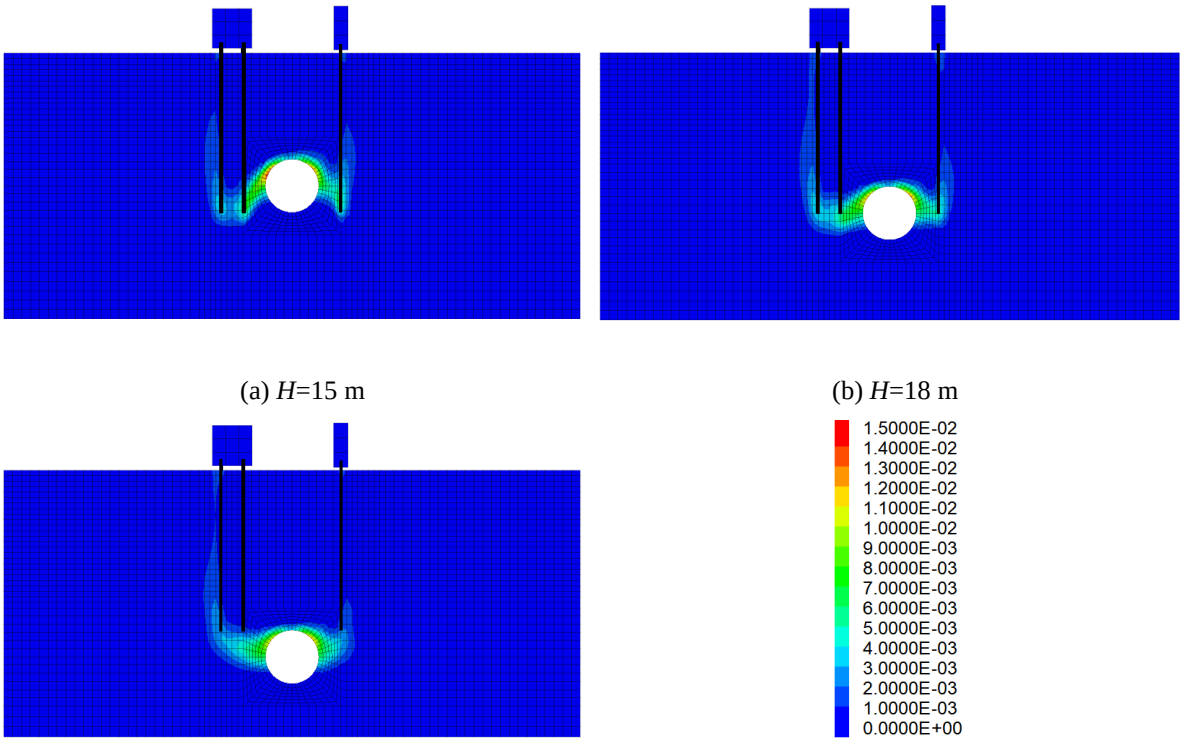

(a) H=15 m (b) H=18 m

(c) H=21 m

Figure 14 Plastic deviator strain contours of the ground induced by tunnelling in Shanghai structured clay

To quantitively describe the disturbances of soil due to tunnelling, the degrees of disturbance related to the fabric anisotropy (R_a), the adhesive mean stress (R_b), and the bonding ratio (R_c) were introduced (see Appendix). The simulated contours of disturbance degrees are presented in Figure 15, Figure 16, and Figure 17. It can be seen that the structural disturbance degree distribution is following the plastic deviator strain distribution. The structural disturbance degree of the anisotropy reaches up to 35% for tunnelling in Shanghai structured clay with 1.0% ground loss, while the induced maximum disturbance degrees of the adhesive mean stress and the bonding ratio are about 3.0% and 8.5%, respectively. Moreover, it is observed that the tunnel depth has a relatively small effect on the magnitude and distribution of the three disturbance degrees.

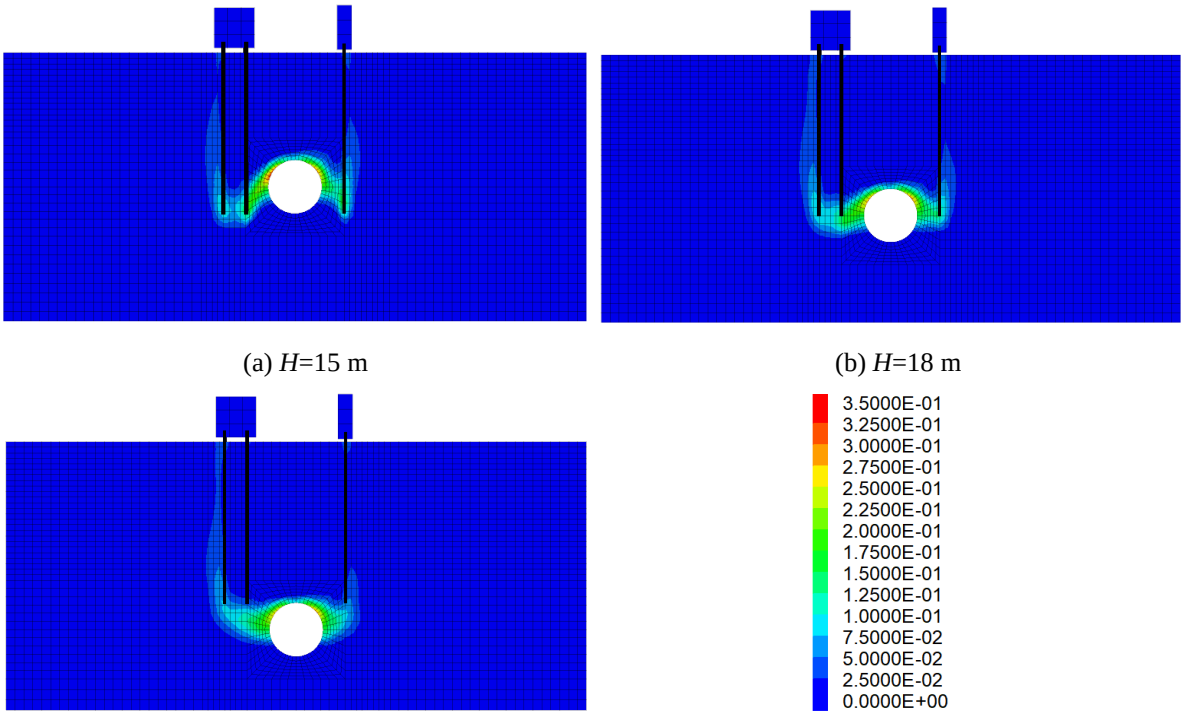

(a) H=15 m (b) H=18 m

(c) H=21 m

Figure 15 Contours of structural disturbance degrees of the anisotropy (R_a) induced by tunnelling in Shanghai structured clay

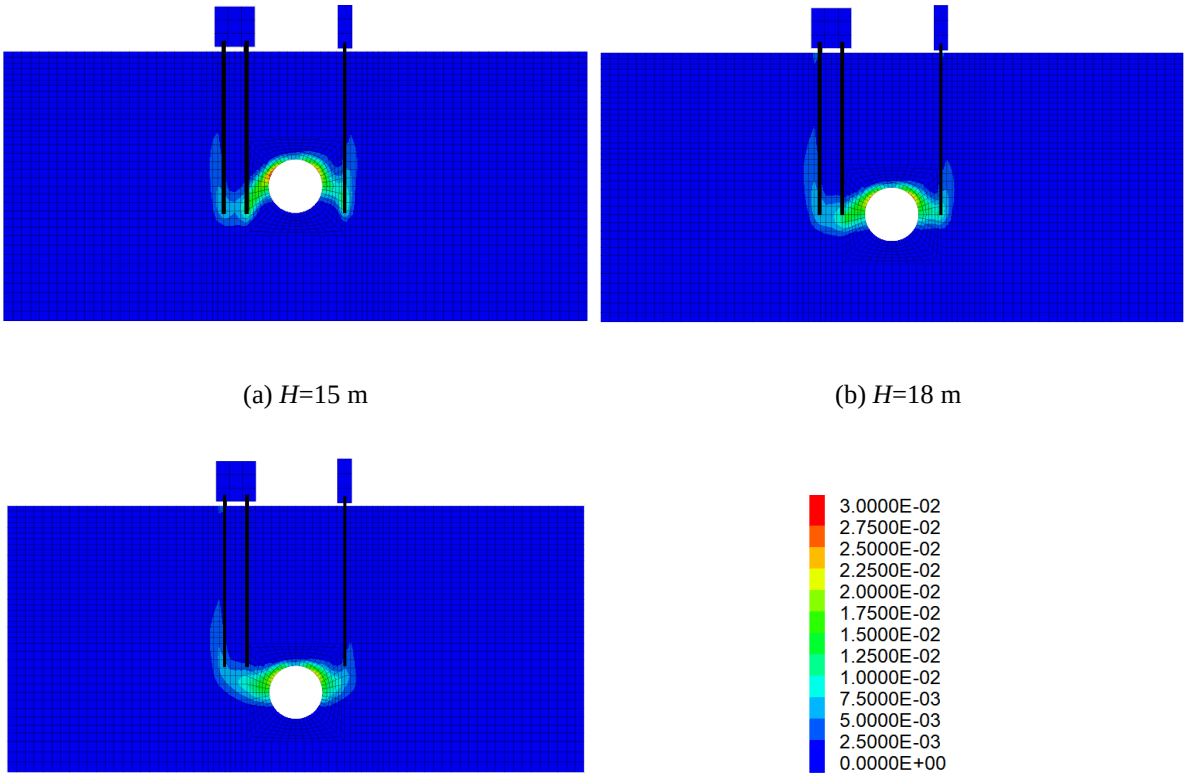

(a) H=15 m (b) H=18 m

(c) H=21 m

Figure 16 Contours of structural disturbance degrees of the adhesive mean stress (R_b) induced by tunnelling in Shanghai structured clay

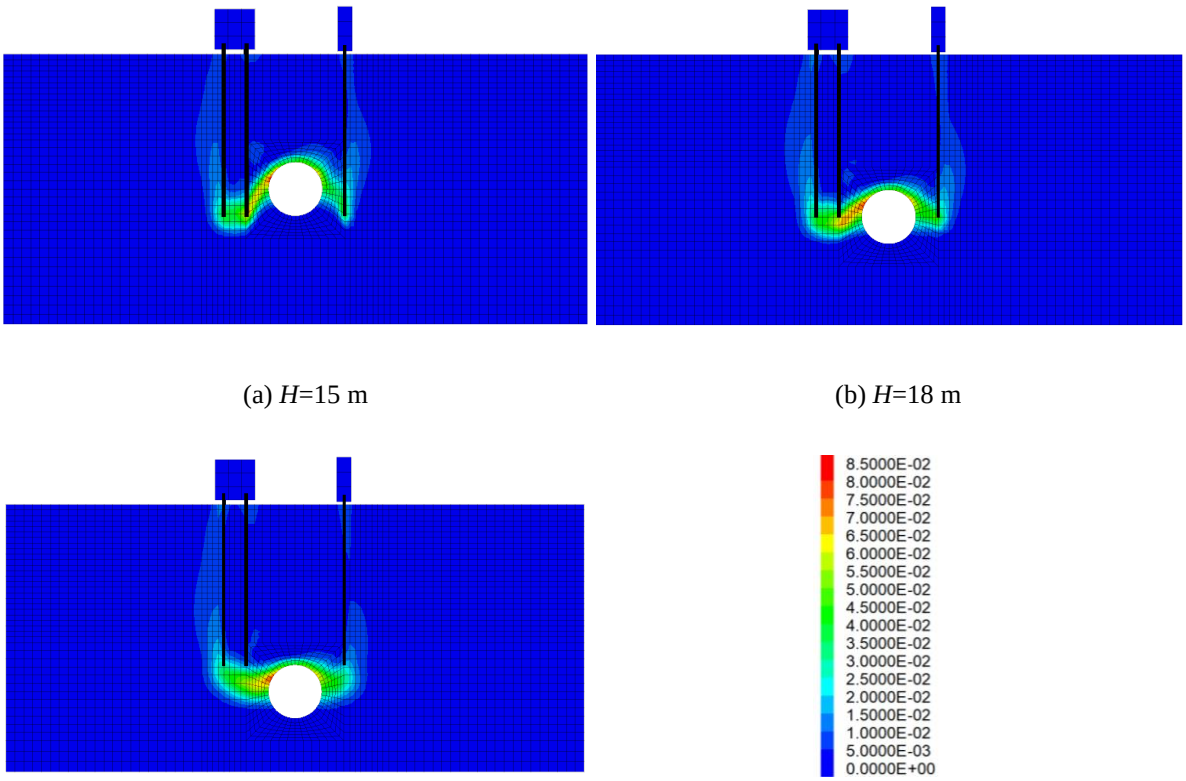

(a) H=15 m (b) H=18 m

(c) H=21 m

Figure 17 Contours of structural disturbance degrees of the bonding ratio (R_c) induced by tunnelling in Shanghai structured clay

5.2. Influences of the anisotropy and the soil structure on the response of tunnelling in Shanghai structured clay

A series of parametric studies have been carried out to investigate the influence of the anisotropy, the bonding ratio, and the adhesive mean stress of soil on the ground and pile movements caused by 1.0% ground loss during tunnelling. As shown in Figure 13, the tunnel axis depth smaller than the pile length is the most critical case regarding the induced bending moment in the piles, so the tunnel axis depth of H = 15 m is chosen for the analysis. The following four situations are analyzed respectively by using: (1) the isotropic ASCM model (equivalent to MCC model), the fully remoulded clay is considered; (2) the anisotropic ASCM model, the anisotropy of clay is considered; (3) the anisotropic structure ASCM model considering the bonding ratio (χ) of clay; (4) the anisotropic structure ASCM model considering the bonding ratio (χ) and the adhesive mean stress (p_b) of undisturbed Shanghai structured clay.

Figure 18 shows the simulated plastic deviator strain contours induced by tunnelling. Figure 19 and Figure 20 show the ground surface and subsurface settlements, respectively. It can be

seen that, compared with the isotropic ground, the introduction of anisotropy decreases the maximum plastic deviator strain, and the ground surface and subsurface settlement. This is because the inclined bounding surface of the anisotropic ASCM model increases the peak shear strength of the soil. The introduction of χ and p_b means the soil is structured clay. The presents of bonding ratio χ indicate that the bounding surface will shrink due to the structural deterioration caused by the disturbance of tunnelling. As a result, the maximum plastic deviator strain, and the ground surface and subsurface settlements are the largest when the bonding ratio χ is considered. The existence of the adhesive mean stress (p_b) will cause the bounding surface to expand, making the soil more difficult to yield stress, leading to a decrease of the maximum plastic deviator strain, and the ground surface and subsurface settlements.

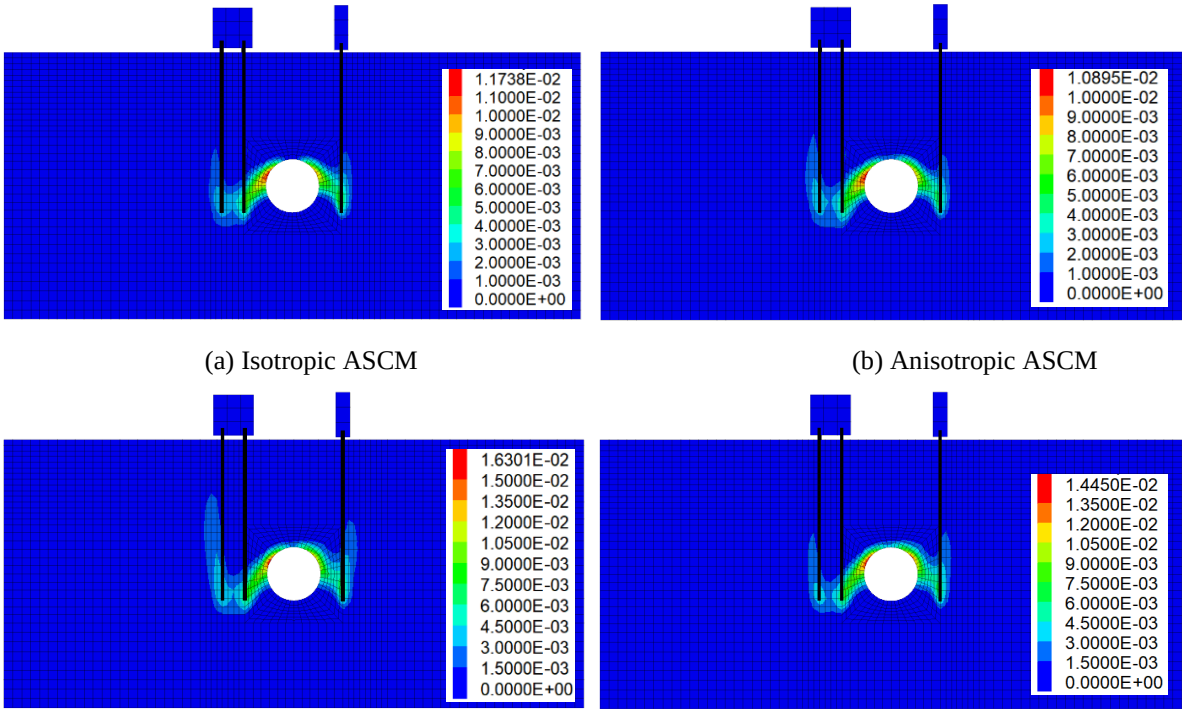

(a) Isotropic ASCM

(b) Anisotropic ASCM

(c) Anisotropic structure ASCM (χ)

(d) Anisotropic structure ASCM (χ, p_b)

Figure 18 Tunnelling-induced plastic deviator strain contours of the ground considering: (a) Isotropic ASCM; (b) Anisotropic ASCM; (c) Anisotropic structure ASCM (χ); (d) Anisotropic structure ASCM (χ, p_b)

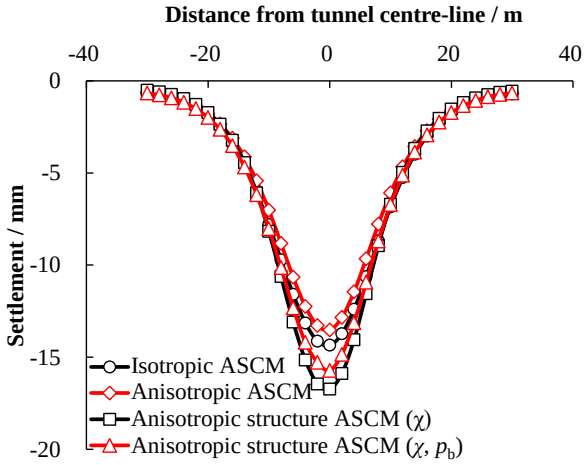

Figure 19 Influences of the anisotropy and the soil structure on tunnelling-induced ground surface settlement

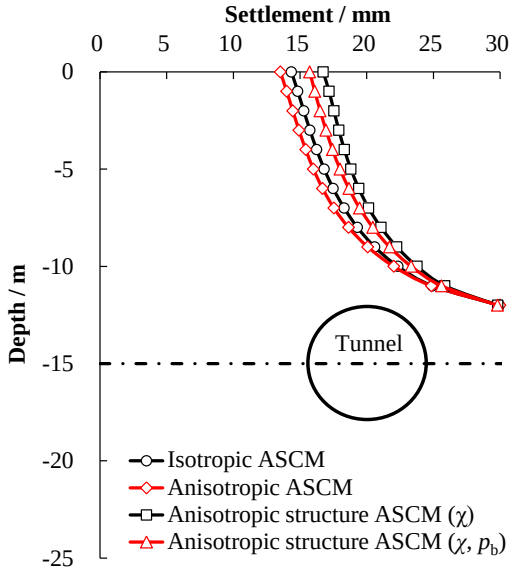

Figure 20 Influences of the anisotropy and the soil structure on tunnelling-induced ground subsurface settlement

Figure 21 presents the tunnelling-induced lateral soil movements. It can be observed that the lateral soil movement of the isotropic ground is basically the same from the depth of the tunnel axis to the crown. The introduction of anisotropy significantly increases the lateral soil movement at the depth of the tunnel axis but has a limited effect on the lateral soil movement at other locations. The introduction of χ leads to a reduction of the lateral soil movement above the tunnel axis, while the presence of p_b also increases the lateral soil movement at the tunnel axis depth.

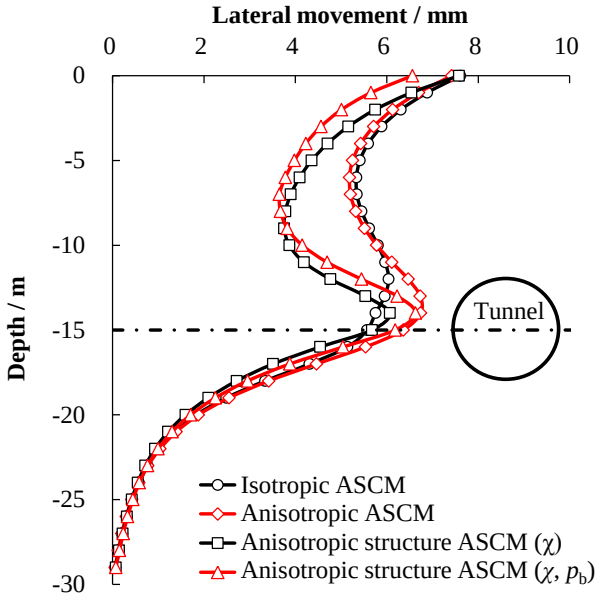

Figure 21 Influences of the anisotropy and the soil structure on tunnelling-induced lateral soil movements

Figure 22 shows the tunnelling-induced lateral movements of the piles. The introduction of anisotropy leads to a slight increase in the lateral movement at the pile bottom, while the introduction of χ significantly reduces the lateral movements of the piles, especially at the upper pile shaft above the tunnel axis where the reduction reaches up to a maximum of about 30%. The presence of p_b reduces slightly the lateral movement at the top of the single pile, while for the front pile and the rear pile, the introduction of p_b increases the lateral movement of the pile shaft above the tunnel axis. Overall, the introduction of the anisotropy, the bonding ratio, and the adhesive mean stress may lead to an increase in the deflection unevenness of the piles.

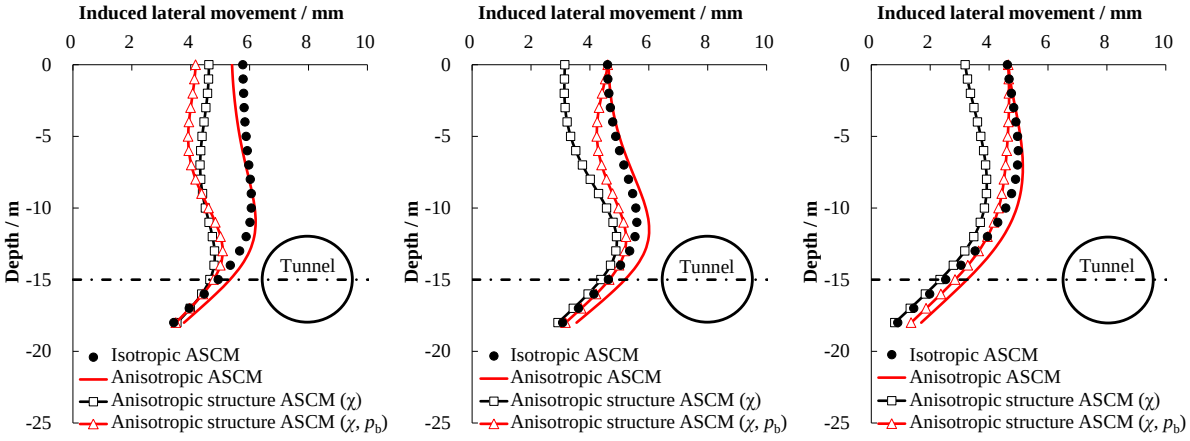

(a) Single pile (b) Front pile (c) Rear pile

Figure 22 Influences of the anisotropy and the soil structure on tunnelling-induced lateral movements of the piles

Figure 23 shows the tunnelling-induced bending moments along the piles. The influence of the anisotropy and the structure of soil on the tunnelling-induced bending moments of the piles corresponds to the deflection of the piles. For the single pile and the front pile, the introduction of the anisotropy and the structure of soil makes the maximum bending moment increase to a maximum of about 60%, while for the rear pile, the influence of soil anisotropy and structure is less significant because the rear pile is relatively far away from the tunnel.

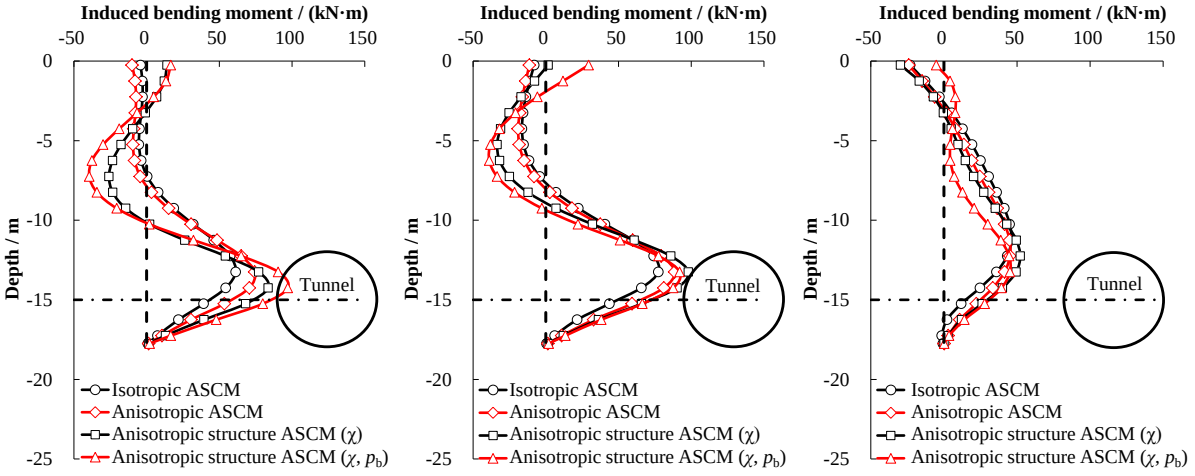

(a) Single pile (b) Front pile (c) Rear pile

Figure 23 Influences of the anisotropy and the soil structure on tunnelling-induced bending moments of the piles

6. Conclusions

In this study, the anisotropic structured clay model (ASCM) has been implemented into FLAC^{3D} through the user-defined constitutive model platform using the coding language of C++. The user-defined ASCM model is firstly calibrated based on the oedometer and undrained triaxial test results for Shanghai structured clay. Then, three-dimensional numerical modellings of centrifuge model tests on the tunnelling-induced ground and pile deformations in remoulded clay have been performed. The computed ground surface settlements, subsurface settlements, soil and pile lateral movements induced by tunnelling agree well with the measurements of the centrifuge model tests, indicating that the three-dimensional numerical model adopting the user-defined ASCM constitutive model is reasonable. Thereafter, the model parameters for Shanghai structured clay have been used to investigate the influences of soil anisotropy and structure on soil-tunnel-pile interaction.

These numerical results should improve the understanding of the origin of risks and damages induced by the degradation of clay structure on the construction of a tunnel near existing piles. The following conclusions can therefore be drawn:

(1) The tunnelling-induced bending moments of piles depend on the relative position of the tunnel and the piles. If the depth of the tunnel is equal to or greater than the pile length, the single and front piles bend away from the tunnel, the absolute maximum bending moments are located in the mid-depth of the pile shaft. While for the case where the tunnel is constructed within the depth of piles, the maximum bending moment is located at the depth of the tunnel due to the tunnelling-induced stress-release. For the studied tunnelling in Shanghai structured clay, the maximum bending moments of the single and front piles are increased from 35 kN·m to 100 kN·m when the depth of tunnel is changed from 3 m below the pile tip to 3 m above the pile tip.

(2) In terms of the influences of the anisotropy and the soil structure on the response of tunnelling, in general, the introduction of the anisotropy, the bonding ratio and the adhesive mean stress will lead to the increase of the plastic deviator strain and the maximum vertical and horizontal movements of the ground responses. For the analysed tunnelling in Shanghai structured clay, compared to the results of the isotropic MCC model, the consideration of soil anisotropy and structure leads to an increase of ground surface settlement and maximum lateral soil movement to a maximum of 9% and 14% respectively. The neglect of soil structure will underestimate the ground movement in engineering practice.

(3) The introduction of the anisotropy, the bonding ratio, and the adhesive mean stress may lead to an increase in the deflection unevenness and the bending moment of the piles. For the analysed tunnelling in Shanghai structured clay where the tunnel depth is smaller than the pile length, compared to the results in reconstituted Shanghai structured clay, the introduction of the anisotropy and the structure of soil makes the maximum bending moment increase to a maximum of about 60%. These numerical results could serve as a reference to update the specifications for design and construction to mitigate and prevent the risks.

Acknowledgement

This research was financially supported by the National Natural Science Foundation of China (Grant Nos. 51608005 and 51579179); and a RIF project (Grant No. R5037-18F) from the Research Grants Council (RGC) of Hong Kong Special Administrative Region Government (HKSARG) of China.

Data Availability Statement

The data that support the findings of this study are available from the corresponding author upon reasonable request.

Competing Interests

we declare that we have no known competing financial interests or personal relationships that could have appeared to influence the work.

Appendix: Anisotropic Structured Clay Model

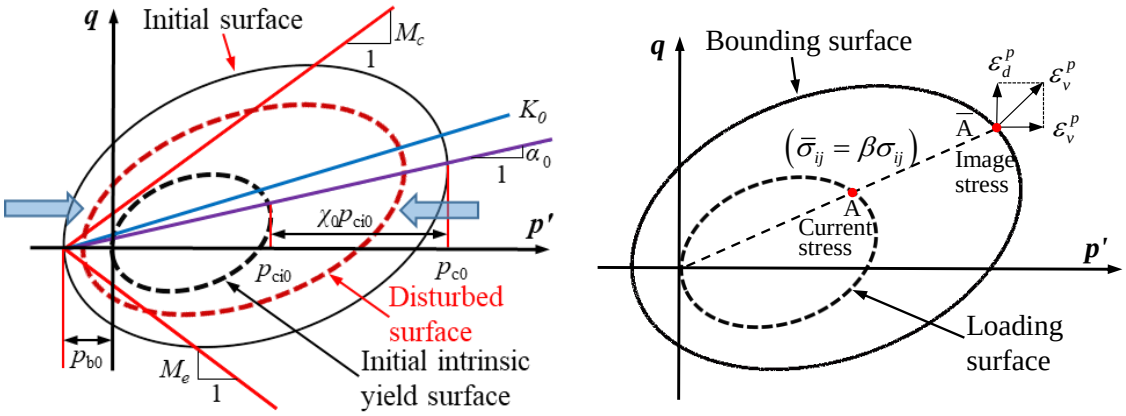

(a) different surfaces (b) mapping rule of bounding surface concept

Figure A1 Schematic plot for the principle of the ASCM model

The elastic behaviour is assumed to be isotropic:

$$\delta\varepsilon_{ij}^{e} = \frac{1+\upsilon}{E}\delta\sigma_{ij} - \frac{\upsilon}{E}\delta\sigma_{kk}\delta_{ij}\text{, with } E = 3K(1-2\upsilon)\text{, } K = \frac{1+e_0}{\kappa}(p' + p_b + \chi p_{ci0}) \quad \text{..... (A1)}$$

where υ, E and K are Poisson's ratio, Young's modulus and bulk modulus; σ'_{ij}, p' are the effective stress tensor and the mean effective stress; δ_{ij} is Kronecker's delta, κ is the slope of the swelling line, e_0 is the initial void ratio. p_b and χp_{ci0} are related to the clay structure.

The bounding surface considering the structure of soil can be expressed as follows:

$$\bar{F}=\frac{3}{2}\frac{\left[\bar{s}_{ij}-\left(\bar{p}+p_b\right)\alpha_{ij}\right]:\left[\bar{s}_{ij}-\left(\bar{p}+p_b\right)\alpha_{ij}\right]}{\left(M\left(\theta\right)^2-\frac{3}{2}\alpha_{ij}:\alpha_{ij}\right)}+\left(\bar{p}+p_b\right)\left[\bar{p}-\left(1+\chi\right)p_{ci}\right]=0 \quad \text{..... (A2)}$$

$$\text{with } M\left(\theta\right)=M_c\left[\frac{2m^4}{\left(1+m^4\right)-\left(1-m^4\right)\sin 3\theta}\right]^{1/4},\ m=M_e/M_c=\frac{3-\sin\phi_c}{3+\sin\phi_c}$$

where $\bar{p}$ and $\bar{s}_{ij}$ are the mean effective and deviatoric stress tensors, respectively, and the bar indicates that these variables are related to the bounding surface; M is the slope of the critical state line in triaxial space, which is related to the Lode angle θ, and the critical state stress ratio for triaxial compression M_c and extension M_e in $p-q$ stress space; ϕ_c is the friction angle with $\phi_c=\sin^{-1}\left[3M_c/\left(6+M_c\right)\right]$; p_{ci}, α_{ij}, p_b and χ are hardening related parameters accounting for the effects of preconsolidation, anisotropy, adhesive stress and bonding of clay:

(1) Isotropic hardening

The hardening parameter p_{ci} reflecting the effect of preconsolidation controls the size of the yield surface according to the plastic volumetric strain rate $\delta\varepsilon_v^p$, given by

$$\delta p_{ci}=p_{ci}\frac{1+e_0}{\lambda-\kappa}\delta\varepsilon_v^p \quad \text{..... (A3)}$$

where λ and κ are the slope of the normal compression line and the slope of the swelling line in the $\log p'-e$ space.

(2) Rotational/anisotropic hardening

For K_0-consolidated reconstituted soils, the initial anisotropy α_{K_0} can be calculated as follows(Wheeler, Näätänen, Karstunen, & Lojander, 2003):

$$\alpha_{K_0} = \eta_{K_0} - \frac{M_c^2 - \eta_{K_0}^2}{3} \quad \text{with } \eta_{K_0} = \frac{3M_c}{6 - M_c} \quad \text{..... (A4)}$$

The rotational hardening law that considers the adhesive mean stress (p_b) of soil, is expressed as follows:

$$\delta\alpha_{ij} = \omega\left[\left(\frac{3s_{ij}}{4p' + 4p_b} - \alpha_{ij}\right)\left\langle\delta\varepsilon_v^p\right\rangle + \omega_d\left(\frac{s_{ij}}{3p' + 3p_b} - \alpha_{ij}\right)\delta\varepsilon_d^p\right] \quad \text{..... (A5)}$$

where $\left\langle\delta\varepsilon_v^p\right\rangle = \delta\varepsilon_v^p$ for $\delta\varepsilon_v^p > 0$ and $\left\langle\delta\varepsilon_v^p\right\rangle = 0$ for $\delta\varepsilon_v^p \le 0$; ω is the absolute rotation rate of the yield surface, and ω_d is the rotation rate of the yield surface related to the deviatoric plastic strain. ω and ω_d can be expressed as follows (Wheeler, Näätänen, Karstunen, & Lojander, 2003; Yang, Yin, Liu, & Gao, 2020; Z.-Y. Yin, Chang, Karstunen, & Hicher, 2010; Z.-Y. Yin, Karstunen, Chang, Koskinen, & Lojander, 2011):

$$\omega = \frac{1 + e_0}{(\lambda - \kappa)} \ln \frac{10M_c^2 - 2\alpha_{K_0}\omega_d}{M_c^2 - 2\alpha_{K_0}\omega_d} \quad \text{..... (A6)}$$

$$\omega_d = \frac{3\left(4M_c{}^2 - 4\eta_{K_0}^2 - 3\eta_{K_0}\right)}{8\left(\eta_{K_0}^2 + 2\eta_{K_0} - M_c{}^2\right)} \quad \text{..... (A7)}$$

The degree of disturbance on the fabric anisotropy (R_a) is defined as follows:

$$R_a = 1 - \exp\left(-\xi_\alpha \varepsilon_d^p\right) \quad \text{..... (A8)}$$

where ξ_α is a model parameter controlling the plastic deviatoric strain effect of the fabric anisotropy to the plastic deviatoric strain ε_d^p , and can be determined by the relation $\xi_\alpha = \omega \cdot \omega_d$.

(3) Adhesive mean stress hardening law

The cementation between natural clay particles makes the soil show adhesive mean stress, p_b, which will be reduced as a result of the structural deterioration of soils caused by plastic strains:

$$p_b = p_{b0} \exp\left(-\xi_b \varepsilon_d^p\right) \quad \text{..... (A9)}$$

where p_{b0} is the initial value of p_b , and ξ_b is a model parameter controlling the degradation rate of the adhesive mean stress related to the plastic deviatoric strain ε_d^p .

The degree of structure disturbance on the adhesive mean stress (R_{b}) is introduced to describe the progressive structural disturbance relating to the adhesive mean stress:

$$R_{\mathrm{b}} = 1 - \exp\left(-\xi_{\mathrm{b}} \varepsilon_{\mathrm{d}}^{\mathrm{p}}\right) \quad \text{(A10)}$$

(4) Bonding ratio hardening law

The bonding ratio χ, which represents the size of the bounding surface relative to the intrinsic yield surface, is used to control the progressive structural deterioration of soils:

$$\chi = \frac{p_{\mathrm{c}}}{p_{\mathrm{ci}}} - 1 \text{ with } \delta\chi = -\chi\xi\left(\left|\delta\varepsilon_{\mathrm{v}}^{\mathrm{p}}\right| + \xi_{\mathrm{d}}\delta\varepsilon_{\mathrm{d}}^{\mathrm{p}}\right) \quad \text{(A11)}$$

where p_{c} and p_{ci} are the sizes of the bounding surface and the intrinsic yield surface, respectively. ξ and ξ_{d} are model parameters controlling the degradation rate of the soil structure related to the plastic volumetric strain increment $\delta\varepsilon_{\mathrm{v}}^{\mathrm{p}}$ and the plastic deviatoric strain increment $\delta\varepsilon_{\mathrm{d}}^{\mathrm{p}}$.

The degree of structure disturbance on the bonding ratio (R_{c}) is introduced to describe the progressive structural deterioration relating to the bonding ratio:

$$R_{\mathrm{c}} = 1 - \exp\left[-\xi\left(\left|\delta\varepsilon_{\mathrm{v}}^{\mathrm{p}}\right| + \xi_{\mathrm{d}}\delta\varepsilon_{\mathrm{d}}^{\mathrm{p}}\right)\right] \quad \text{(A12)}$$

For naturally deposited clays, the initial size of the bounding surface p_{c0} and the intrinsic yield surface p_{ci0} varies with depth and can be determined by

$$p_{\mathrm{c0}} = \frac{\left[q_0 - \left(p_0^{'} + p_{\mathrm{b0}}\right)\alpha_{K_0}\right]^2}{\left(M_{\mathrm{c}}^2 - \alpha_{K_0}^2\right)\left(p_0^{'} + p_{\mathrm{b0}}\right)} + p_0^{'} \quad \text{(A13)}$$

$$p_{\mathrm{ci0}} = \frac{p_{\mathrm{c0}}}{1 + \chi_0} \quad \text{(A14)}$$

where $p_0^{'} = \left|2\sigma_x^{'} + \sigma_z^{'} + (1 + 2K_0)\cdot POP\right| / 3$, $q_0 = \left|\sigma_z^{'} - \sigma_x^{'} + \left(1 - K_0\right)\cdot POP\right|$, $\sigma_x^{'}$ and $\sigma_z^{'}$ are the horizontal and vertical effective stress that varies with depth.

The linear mapping rule (Y. Dafalias, 1982) between the current stress σ_{ij} and those at the bounding surface $\bar{\sigma}_{ij}$ is illustrated in Figure A1, with the projection centre fixed at the origin of $p'-q$ space and β is the mapping coefficient:

$$\bar{\sigma}_{ij} = \beta \sigma_{ij} \quad \text{(A15)}$$

The plastic strain inside the bounding surface can be determined as (Manzari & Nour, 1997):

$$\delta\varepsilon_{ij}^{\mathrm{p}} = \mathrm{d}\lambda \frac{\partial \bar{F}}{\partial \bar{\sigma}_{ij}} \quad \text{with} \quad \mathrm{d}\lambda = \frac{1}{K_{\mathrm{p}}} \frac{\partial \bar{F}}{\partial \bar{\sigma}_{ij}} \delta\sigma_{ij} = \frac{1}{\bar{K}_{\mathrm{p}}} \frac{\partial \bar{F}}{\partial \bar{\sigma}_{ij}} \delta\bar{\sigma}_{ij} \quad \text{(A16)}$$

where K_{p} and $\bar{K}_{\mathrm{p}}$ are the plastic modulus of the current loading surface and the bounding surface, respectively. The plastic modulus is represented by the distance between the current stress state and its projection on the bounding surface (Y. F. Dafalias, 1986):

$$K_{\mathrm{p}} = \bar{K}_{\mathrm{p}} + k_{\mathrm{p}} \frac{1+e_0}{\lambda-\kappa} (\beta p')^3 \cdot (1-\frac{1}{\beta}) \quad \text{(A17)}$$

where K_{p} is a scalar depending on the vector length of the current stress state point to the projection point on the bounding surface; k_{p} is a constant for the plastic modulus.

References

Clayton, C. R. I., Hight, D. W., & Hopper, R. J. (1992). Progressive destructuring of Bothkennar clay: implications for sampling and reconsolidation procedures. *Géotechnique, 42*(2), 219-239

Dafalias, Y. (1982). Bounding surface formulation of soil plasticity. *Soil mechanics-transient and cyclic loads*, 253-282

Dafalias, Y. F. (1986). Bounding Surface Plasticity. I: Mathematical Foundation and Hypoplasticity. *Journal of Engineering Mechanics, 112*(9), 966-987. doi: doi:10.1061/(ASCE)0733-9399(1986)112:9(966)

Divall, S. (2013). Ground movements associated with twin-tunnel construction in clay. *Ph. D. thesis. City University London, London.*

Hong, Y., Soomro, M. A., & Ng, C. W. W. (2015). Settlement and load transfer mechanism of pile group due to side-by-side twin tunnelling. *Computers and Geotechnics, 64*, 105-119. doi: 10.1016/j.compgeo.2014.10.007

Huang, M., Liu, Y., & Sheng, D. (2011). Simulation of yielding and stress–stain behavior of shanghai soft clay. *Computers and Geotechnics, 38*(3), 341-353

Itasca Consulting Group Inc. (2018). Fast Lagrangian analysis of continua in three dimensions, Version 6.0. *User's Guide, Minneapolis, Minnesota, USA*

Jiang, M., & Yin, Z.-Y. (2012). Analysis of stress redistribution in soil and earth pressure on tunnel lining using the discrete element method. *Tunnelling and Underground Space Technology, 32*, 251-259
Jiang, M., & Yin, Z.-Y. (2014). Influence of soil conditioning on ground deformation during longitudinal tunneling. *Comptes Rendus Mecanique, 342*(3), 189-197
Jin, Y.-F., Yin, Z.-Y., Zhou, W.-H., & Horpibulsuk, S. (2019). Identifying parameters of advanced soil models using an enhanced transitional Markov chain Monte Carlo method. *Acta Geotechnica, 14*(6), 1925-1947
Jin, Y.-F., Yin, Z.-Y., Zhou, W.-H., & Huang, H.-W. (2019). Multi-objective optimization-based updating of predictions during excavation. *Engineering Applications of Artificial Intelligence, 78*, 102-123
Jin, Y. F., Yin, Z. Y., Shen, S. L., & Hicher, P. Y. (2016). Selection of sand models and identification of parameters using an enhanced genetic algorithm. *International Journal for Numerical and Analytical Methods in Geomechanics, 40*(8), 1219-1240
Jin, Y. F., Yin, Z. Y., Zhou, W. H., & Shao, J. F. (2019). Bayesian model selection for sand with generalization ability evaluation. *International Journal for Numerical and Analytical Methods in Geomechanics, 43*(14), 2305-2327
Lee, K. M., Rowe, R. K., & Lo, K. Y. (1992). Subsidence owing to tunnelling. I. Estimating the gap parameter. *Canadian Geotechnical Journal, 29*(6), 929-940
Leroueil, S., & Vaughan, P. R. (1990). The general and congruent effects of structure in natural soils and weak rocks. *Géotechnique, 40*(3), 467-488
Li, P., Du, S.-J., Ma, X.-F., Yin, Z.-Y., & Shen, S.-L. (2014). Centrifuge investigation into the effect of new shield tunnelling on an existing underlying large-diameter tunnel. *Tunnelling and Underground Space Technology, 42*, 59-66
Liu, M. D., & Carter, J. P. (2002). A structured Cam Clay model. *Canadian Geotechnical Journal, 39*(6), 1313-1332. doi: 10.1139/t02-069
Loganathan, N., Poulos, H. G., & Stewart, D. P. (2000). Centrifuge model testing of tunnelling-induced ground and pile deformations. *Géotechnique, 50*(3), 283-294
Loganathan, N., Poulos, H. G., & Xu, K. J. (2001). Ground and Pile-Group Responses Due to Tunnelling. *Soils and Foundations, 41*(1), 57-67. doi: 10.3208/sandf.41.57
Lu, H., Shi, J., Ng, C. W. W., & Lv, Y. (2020). Three-dimensional centrifuge modeling of the influence of side-by-side twin tunneling on a piled raft. *Tunnelling and Underground Space Technology, 103*. doi: 10.1016/j.tust.2020.103486
Manzari, M. T., & Nour, M. A. (1997). On implicit integration of bounding surface plasticity models. *Computers & Structures, 63*(3), 385-395
Marshall, A. M., & Mair, R. J. (2011). Tunneling beneath driven or jacked end-bearing piles in sand. *Canadian Geotechnical Journal, 48*(12), 1757-1771. doi: 10.1139/t11-067
Ng, C. W. W., Hong, Y., & Soomro, M. A. (2015). Effects of piggyback twin tunnelling on a pile group: 3D centrifuge tests and numerical modelling. *Géotechnique, 65*(1), 38-51. doi: 10.1680/geot.14.P.105
Ng, C. W. W., & Lu, H. (2014). Effects of the construction sequence of twin tunnels at different depths on an existing pile. *Canadian Geotechnical Journal, 51*(2), 173-183. doi: 10.1139/cgj-2012-0452
Ng, C. W. W., Soomro, M. A., & Hong, Y. (2014). Three-dimensional centrifuge modelling of pile group responses to side-by-side twin tunnelling. *Tunnelling and Underground Space Technology, 43*, 350-361. doi: 10.1016/j.tust.2014.05.002
Shen, S.-L., Wu, H.-N., Cui, Y.-J., & Yin, Z.-Y. (2014). Long-term settlement behaviour of metro tunnels in the soft deposits of Shanghai. *Tunnelling and Underground Space Technology, 40*( ), 309-323. doi: https://doi.org/10.1016/j.tust.2013.10.013

Soomro, M. A., Hong, Y., Ng, C. W. W., Lu, H., & Peng, S. (2015). Load transfer mechanism in pile group due to single tunnel advancement in stiff clay. *Tunnelling and Underground Space Technology, 45*, 63-72. doi: 10.1016/j.tust.2014.08.001

Soomro, M. A., Kumar, M., Xiong, H., Mangnejo, D. A., & Mangi, N. (2020). Investigation of effects of different construction sequences on settlement and load transfer mechanism of single pile due to twin stacked tunnelling. *Tunnelling and Underground Space Technology, 96*. doi: 10.1016/j.tust.2019.103171

Soomro, M. A., Mangi, N., Xiong, H., Kumar, M., & Mangnejo, D. A. (2020). Centrifuge and numerical modelling of stress transfer mechanisms and settlement of pile group due to twin stacked tunnelling with different construction sequences. *Computers and Geotechnics, 121*, 23. doi: 10.1016/j.compgeo.2020.103449

Soomro, M. A., Ng, C. W. W., Liu, K., & Memon, N. A. (2017). Pile responses to side-by-side twin tunnelling in stiff clay: Effects of different tunnel depths relative to pile. *Computers and Geotechnics, 84*, 101-116. doi: 10.1016/j.compgeo.2016.11.011

Wheeler, S. J., Näätänen, A., Karstunen, M., & Lojander, M. (2003). An anisotropic elastoplastic model for soft clays. *Canadian Geotechnical Journal, 40*(2), 403-418. doi: 10.1139/t02-119

Williamson, M. G., Elshafie, M. Z. E. B., Mair, R. J., & Devriendt, M. D. (2017). Open-face tunnelling effects on non-displacement piles in clay – part 1: centrifuge modelling techniques. *Géotechnique, 67*(11), 983-1000. doi: 10.1680/jgeot.sip17.P.119

Williamson, M. G., Mair, R. J., Devriendt, M. D., & Elshafie, M. Z. E. B. (2017). Open-face tunnelling effects on non-displacement piles in clay – part 2: tunnelling beneath loaded piles and analytical modelling. *Géotechnique, 67*(11), 1001-1019. doi: 10.1680/jgeot.SIP17.P.120

Wongsaroj, J., Soga, K., & Mair, R. (2013). Tunnelling-induced consolidation settlements in London Clay. *Géotechnique, 63*(13), 1103

Wu, H.-N., Shen, S.-L., Chai, J.-C., Zhang, D.-M., & Xu, Y.-S. (2014). Evaluation of train-load-induced settlement in metro tunnels. *Proceedings of the Institution of Civil Engineers-Geotechnical Engineering, 168*(5), 396-406

Yang, J., Yin, Z.-Y., Laouafa, F., & Hicher, P.-Y. (2019a). Analysis of suffusion in cohesionless soils with randomly distributed porosity and fines content. *Computers and Geotechnics, 111*, 157-171. doi: 10.1016/j.compgeo.2019.03.011

Yang, J., Yin, Z.-Y., Laouafa, F., & Hicher, P.-Y. (2019b). Hydromechanical modeling of granular soils considering internal erosion. *Canadian Geotechnical Journal, 57*(2), 157-172. doi: 10.1139/cgj-2018-0653

Yang, J., Yin, Z.-Y., Laouafa, F., & Hicher, P.-Y. (2019c). Modeling coupled erosion and filtration of fine particles in granular media. *Acta Geotechnica, 14*(6), 1615-1627. doi: 10.1007/s11440-019-00808-8

Yang, J., Yin, Z.-Y., Liu, X.-F., & Gao, F.-P. (2020). Numerical analysis for the role of soil properties to the load transfer in clay foundation due to the traffic load of the metro tunnel. *Transportation Geotechnics, 23*, 100336. doi: 10.1016/j.trgeo.2020.100336

Yang, J., Yin, Z. Y., Laouafa, F., & Hicher, P. Y. (2019). Internal erosion in dike ‐ on ‐ foundation modeled by a coupled hydromechanical approach. *International Journal for Numerical and Analytical Methods in Geomechanics, 43*(3), 663-683. doi: 10.1002/nag.2877

Yin, Z.-Y., Chang, C. S., Karstunen, M., & Hicher, P.-Y. (2010). An anisotropic elastic–viscoplastic model for soft clays. *International Journal of Solids and Structures, 47*(5), 665-677. doi: 10.1016/j.ijsolstr.2009.11.004

Yin, Z.-Y., Jin, Y.-F., Shen, S.-L., & Huang, H.-W. (2017). An efficient optimization method for identifying parameters of soft structured clay by an enhanced genetic algorithm and elastic–viscoplastic model. *Acta Geotechnica, 12*(4), 849-867

Yin, Z.-Y., Karstunen, M., Chang, C. S., Koskinen, M., & Lojander, M. (2011). Modeling Time-Dependent Behavior of Soft Sensitive Clay. *Journal of Geotechnical and Geoenvironmental Engineering, 137*(11), 1103-1113. doi: 10.1061/(asce)gt.1943-5606.0000527

Yin, Z.-Y., Xu, Q., & Hicher, P.-Y. (2013). A simple critical-state-based double-yield-surface model for clay behavior under complex loading. *Acta Geotechnica, 8*(5), 509-523

Yin, Z. Y., Jin, Y. F., Shen, J. S., & Hicher, P. Y. (2018). Optimization techniques for identifying soil parameters in geotechnical engineering: Comparative study and enhancement. *International Journal for Numerical and Analytical Methods in Geomechanics, 42*(1), 70-94

Zhang, D., Huang, Z., Yin, Z., Ran, L., & Huang, H. (2017). Predicting the grouting effect on leakage-induced tunnels and ground response in saturated soils. *Tunnelling and Underground Space Technology, 65*, 76-90

Figure captions

Figure 1 General calculation cycle with a user-defined constitutive model in FLAC3D

Figure 2 Simulation of oedometer test on Shanghai clay

Figure 3 Simulation of undrained triaxial tests on isotropically consolidated Shanghai structured clay

Figure 4 Simulation of undrained triaxial tests on *K0* consolidated Shanghai structured clay

Figure 5 Detail and geometry of the centrifuge model (N. Loganathan, Poulos, & Stewart, 2000)

Figure 6 Numerical model of the tunnel and piles (for the case of test 2, H = 18 m)

Figure 7 Measured and computed undrained shear strength profiles of the clay

Figure 8 Non-uniform boundary contraction model

Figure 9 Measured and computed ground surface settlement induced by tunnelling for different tunnel buried depths

Figure 10 Measured and computed subsurface settlement of the ground induced by tunnelling

Figure 11 Measured and computed lateral soil movements induced by tunnelling at different depths